JOURNAL OF VIROLOGY, Aug. 2006, p. 7909–7917 Vol. 80, No. 16
0022-538X/06/$08.00+0 doi:10.1128/JVI.00525-06

New Antiviral Target Revealed by the Hexameric Structure of Mouse Hepatitis Virus Nonstructural Protein nsp15

Xiaoling Xu,[1,2]† Yujia Zhai,[1,2]† Fei Sun,[1,2] Zhiyong Lou,[1,2] Dan Su,[1,2] Yuanyuan Xu,[1,2] Rongguang Zhang,[2,3] Andrzej Joachimiak,[3] Xuejun C. Zhang,[2,4] Mark Bartlam,[1,2] and Zihe Rao[1,2]*

"Tsinghua-IBP Joint Research Group for Structural Biology," Tsinghua University, Beijing 100084, China[1]; National Laboratory of Biomacromolecules, Institute of Biophysics (IBP), Chinese Academy of Sciences, Beijing 100101, China[2]; Biosciences Division, Argonne National Laboratory, Argonne, Illinois 60439[3]; and Crystallography Research Program, Oklahoma Medical Research Foundation, Oklahoma City, Oklahoma 73104[4]

Received 14 March 2006/Accepted 2 May 2006

The unique coronavirus transcription/replication machinery comprised of multiple virus-encoded nonstructural proteins (nsp) plays a vital role during initial and intermediate phases of the viral life cycle. The crystal structure of mouse hepatitis virus strain A59 (MHV-A59) nsp15 is reported at 2.15-Å resolution. nsp15 is an XendoU endoribonuclease and is the first one from this family to have its structure unveiled. The MHV-A59 nsp15 monomer structure has a novel protein fold. Two nsp15 trimers form a back-to-back hexamer that is believed to be the functional unit. The structure reveals the catalytic site including the highly conserved residues His262, His277, and Lys317, which is supported by mutagenesis analysis. Gel filtration and enzyme activity assays confirmed that the hexamer is the active form for nsp15 and demonstrate the specificity of nsp15 for uridylate. The high sequence conservation of nsp15 in coronaviruses, including that of severe acute respiratory syndrome, suggests that this protein may provide a new target for the design of antiviral therapeutics.

Mouse hepatitis virus (MHV) belongs to group II of the genus *Coronavirus* (CoV), together with bovine coronavirus, human coronavirus strain OC43, and the recently identified severe acute respiratory syndrome coronavirus (SARS-CoV) (2). The two strains of MHV that have been extensively studied to date are A59 (MHV-A59) and JHM (MHV-JHM or MHV-4). These coronavirus strains cause a variety of diseases in susceptible mice, such as enteritis, hepatitis, and panencephalitis, with acute and chronic demyelination that is histologically similar to multiple sclerosis in humans (13, 14). Much of our knowledge concerning the replication mechanism of coronaviruses has been acquired from the use of MHV as a model for pathogenesis, docking and entry, receptor usage, transcription, replication, polymerase function, assembly, and release (31). MHV-A59 in particular is used extensively as a model to study the role of the immune system in virus-induced ventral nervous system demyelination. To date, the pathology of demyelination is still not clear; thus, further insights into the replication and transcription of the model are required to better use this model for further study of demyelination, replication, and transcription of other coronaviruses.

MHV-A59 is a positive-strand RNA coronavirus with a genome of 31 kb in length, of which about 22 kb is encompassed by the replicase gene containing two large overlapping open reading frames (ORF), termed ORF1a and ORF1b. The replicase gene expresses two large polyproteins, pp1a (495 kDa) and pp1ab (803 kDa), where expression of pp1ab involves a −1 ribosomal frameshift just upstream of the ORF1a translation termination codon (31). Neither pp1a nor pp1ab is detected intact in MHV-infected cells, since they are cotranslationally and posttranslationally processed by three proteases (two papain-like proteases, PLP1 and PLP2, and a main protease, M^{pro}) into at least 14 mature nonstructural proteins (1, 23, 29). These nonstructural proteins assemble into a large membrane-anchored replicase-transcriptase protein complex, or replicase-transcriptase for short, although their roles in replication and pathogenesis are not entirely clear. Among the nonstructural proteins, nsp14, nsp15, and nsp16 are predicted to be a putative 3′ to 5′ exonuclease, endoribonuclease, and 2′-O RNA methytransferase, respectively. It is conceivable that they, alone or in concert with other enzymes like RNA-dependent RNA polymerase (nsp12) and helicase (nsp13), are involved in viral RNA synthesis, particularly in transcription (23). One hypothesis is that an endoribonuclease activity is required in minus-strand RNA synthesis to digest the nascent RNA and disassemble the ternary complex prior to the translocation of the ternary polymerase complex (3, 9, 10).

Structural studies of coronavirus proteins have mainly been focused on SARS-CoV, and the crystal structures of five nonstructural proteins have so far been determined (2). nsp5, also called the main protease (M^{pro}) or 3C-like protease ($3CL^{pro}$), was the first SARS protein structure to be determined in 2003 (30). A broad-spectrum inhibitor has since been reported with efficient in vitro inactivation of multiple coronavirus M^{pro}s, including that of SARS-CoV, as well as having potent antiviral activity and extremely low cellular toxicity (29). The structure of nsp9, determined in 2004, confirmed its function as a single-strand RNA binding protein (6, 26). The ADP ribose 1-phos-

* Corresponding author. Mailing address: Laboratory of Structural Biology, Life Sciences Building, Tsinghua University, Beijing 100084, China. Phone: 86 10 62771493. Fax: 86 10 62773145. E-mail: raozh@xtal.tsinghua.edu.cn.

† These authors made equal contributions.

phatase (ADRP) domain of nsp3 was reported recently (22), as was the hexadecameric complex structure between nsp7 and nsp8 that should constitute a processivity factor for nsp12, the RNA-dependent RNA polymerase (32). More recently, the structure of nsp10 has been determined and found to belong to a new class of zinc finger proteins (D. Su and Z. Rao, unpublished results). However, no structure of the three putative RNA processing enzymes (nsp14, nsp15, and nsp16) has been reported to date.

The nsp15 proteins from MHV-A59, SARS-CoV, bovine CoV-Lun, human CoV-229E, and avian infectious bronchiolitis virus type B, along with equine torovirus pp1b, gill-associated virus pp1b, equine arteritis virus nsp11, and porcine reproductive and respiratory syndrome virus nsp11, all belong to the XendoU family and possess endoribonuclease activity (23). XendoU is named after a novel endoribonuclease from *Xenopus laevis* oocyte nuclear extracts involved in the processing of the intron-encoded box C/D U16 small nuclear RNA from its pre-mRNA (12). It has been shown that XendoU (e.g., SARS-CoV nsp15) (3) and NendoU (10) share functional characteristics, in that both are Mn^{2+}-dependent endoribonucleases with cleavage specificity for single- and double-stranded RNA 5′ of uridine nucleotides to produce a 2′-3′-cyclic phosphate end product. Whether MHV nsp15 possesses identical activity remains to be demonstrated. Biochemical studies of SARS-CoV nsp15 show that it exists in equilibrium between hexamers and monomers in solution. Hexamers are the dominant species at micromolar protein concentrations, and only this oligomeric state of nsp15 is functional (9). Transmission electron microscopic (EM) analysis further revealed that the six subunits of the hexamer were arranged as a dimer of trimers with a number of cavities or channels that may constitute RNA binding sites (9). However, no high-resolution three-dimensional (3D) structure of any member of the XendoU family has been reported to date.

With regard to the conservation of endoribonuclease activity in the XendoU family and the unusual RNA synthesis mechanism of coronaviruses, MHV-A59 nsp15 will serve as a model for both structural and functional studies. Here we report the hexameric crystal structure of wild-type MHV-A59 nsp15 at 2.7-Å resolution and the MHV-A59 nsp15 F307L mutant at 2.15-Å resolution. Furthermore, enzyme activity assays reveal that MHV-A59 nsp15 is indeed a uridine-specific RNA endonuclease whose activity is enhanced by manganese ions. Site-directed mutagenesis analysis indicates that the vital active-site residues of MHV-A59 nsp15 include His262, His277, and Lys317, which are conserved across the entire XendoU/NendoU family and may play a role in enzyme catalysis (23). We also found that the enzyme activity is correlated with the oligomerization state of MHV-A59 nsp15 and that the active form should be the hexamer but not the monomer.

MATERIALS AND METHODS

Protein expression and purification. The complete gene fragment encoding MHV-A59 nsp15 was cloned from the virus RNA genome by reverse transcription-PCR into the pGEX6p-1 vector (Amersham Biosciences), and the resulting plasmid was transformed into *Escherichia coli* BL21(DE3) cells. The recombinant glutathione *S*-transferase (GST) fusion protein, GST-nsp15, was purified by GST-glutathione affinity chromatography. The GST tag was removed by PreScission protease (Amersham Biosciences), leading to five additional residues (GPLGS) at the N terminus. It was noted that the expression of the wild-type (WT) nsp15 is toxic to *E. coli*, indicated by slower cell growth and low yield. An incidental F307L point mutation was identified because of its significantly improved expression under the same conditions as those of the WT. In addition, another three mutants, H262S, H277S, and K317S, were constructed, expressed, and purified using the same protocol; all resulted in higher yields than the WT nsp15.

Crystallization. MHV-A59 nsp15 was crystallized by the hanging drop vapor diffusion method with a 3-μl drop volume. A 1.5-μl mixture of nsp15 at 10 mg/ml and the *n*-octyl β-D-thioglucopyranoside (OTG) detergent at a final concentration of 6 mM was added to the same volume of reservoir solution (0.6 to 1.0 M lithium sulfate, 0.5 M ammonium sulfate, and 0.1 M sodium citrate, pH 6.0), producing drum-shaped crystals with the space group $P6_322$. Crystals grown under the same conditions but without the OTG detergent had a thin semicircular shape and diffracted poorly in the c^* direction.

Data collection. To improve their diffraction quality, the drum-like crystals of WT nsp15 were dehydrated in a buffer containing 0.2 M lithium sulfate, 3 M ammonium sulfate, 0.1 M sodium citrate (pH 6.0), 4% glycerol for 10 to 20 min and then transferred to a cryoprotectant solution that contained the same components as the dehydration buffer but with a lower concentration of ammonium sulfate (1 M) (to avoid forming salt crystals) and a higher concentration of glycerol (25%). A 2.7-Å-resolution data set of WT nsp15 was collected at 100 K using an in-house Rigaku MM-007 generator and a Rigaku R-AXIS IV++ detector. The crystal form belongs to the hexagonal space group $P6_322$ ($a = b =$ 86.4 Å, c = 221.1 Å, $\alpha = \beta = 90°$, $\gamma = 120°$) with one copy of nsp15 per asymmetric unit and a V_M of 2.8 $Å^3$ Da^{-1} (5, 15), corresponding to a solvent content of 57%.

Crystals of the selenomethionyl (Se-Met) derivative F307L mutant were obtained in order to solve the phase problem. The Se-Met crystals shared the same space group and unit cell with the WT crystals and were dehydrated and cryoprotected following the same protocol. The F307L mutant of nsp15 was used, as it is easier to express than the wild type under the same conditions. A 2.15-Å-resolution data set of the Se-Met derivative was collected for the F307L mutant at 100 K using an SBC2 (3,000 by 3,000) CCD detector on beamline BL19-ID at the Advanced Photon Source (Argonne National Laboratory). Processing of diffraction images and scaling of the integrated intensities were performed using the HKL2000 software package (18).

Structure determination. The structure of nsp15 was solved by the single-wavelength anomalous dispersion (SAD) method from an Se-Met derivative of the F307L mutant. Four of the five potential selenium atoms in one nsp15 monomer were located, and initial phases were calculated by the program SOLVE (27). Density modification (solvent flipping) and phase extension to 2.15 Å were performed using RESOLVE (27). The model of nsp15 was automatically traced using the program ARP/wARP (19) to approximately 80% completeness and then further manually built and refined using the programs O (11) and CNS (4). The F307L mutant crystal structure was refined at 2.15-Å resolution to a final R_{work} of 20.8% and R_{free} of 24.8%. The WT nsp15 structure was refined at 2.7-Å resolution to a final R_{work} of 19.5% and R_{free} of 25.7%. Refinement statistics are detailed in Table 1.

Gel filtration. The oligomerization of MHV-A59 nsp15 was analyzed by eluting the nsp15 protein from a Superdex 200 HR10/30 gel filtration column (Pharmacia) with a buffer containing 25 mM Tris-HCl (pH 8.0), 150 mM NaCl, 1 mM dithiothreitol (DTT) at a flow rate of 0.5 ml min^{-1} and temperature of 16°C. The WT and mutants (H262S, H277S, K317S, and F307L) were analyzed in parallel under the same buffer conditions. All experiments were repeated more than three times, and representative data are shown.

Enzyme activity assay. The activity of MHV-A59 nsp15 was examined using fluorescent resonance energy transformation (FRET) (24, 25) following a previously published protocol (17). Two substrates were designed based on the core MHV transcription regulatory sequence (5′-UCUAAAC-3′) (9, 33); each contains a 6-carboxyfluorescein (6-FAM) and a tetramethylrhodamine (TAMRA) group linked respectively to the 5′ end and 3′ end of a four-nucleotide substrate. One substrate consists of the nucleotides dC-rU-dA-dA, and the other consists of dC-dT-dA-dA as a negative control. The excitation and emission wavelengths of 6-FAM are 498 nm and 518 nm, respectively; those of TAMRA are 558 nm and 576 nm, respectively. While the physical closeness of the 6-FAM and TAMRA groups in the intact substrate diminishes fluorescent emission at 518 nm, cleavage of the substrate dC-rU-dA-dA at the ribonucleotide uridine separates the two fluorophore groups and results in an increase in the 518-nm emission. Activity assays for WT nsp15 and H262S, H277S, K317S, and F307L mutants were performed under the same conditions in a buffer containing 50 mM HEPES (pH 7.5) and 50 mM KCl, which was diluted by 0.1% diethyl pyrocarbonate-treated water. The activity was assayed at 30°C, with the excitation wavelength at 485 nm and emission wavelength at 518 nm, using a fluorescence time scan with

TABLE 1. Data collection and refinement statistics

Statistical element	Mutant Se-nsp15 F307L	WT nsp15
Data collection statistics		
Cell parameters	$a = b = 86.4$ Å, $c = 221.1$ Å, $\alpha = \beta = 90°$, $\gamma = 120°$	$a = b = 86.4$ Å, $c = 221.1$ Å, $\alpha = \beta = 90°$, $\gamma = 120°$
Space group	$P6_322$	$P6_322$
Wavelength used (Å)	0.9798	1.5418
Resolution (Å)	50 (2.25)[c]–2.15	50 (2.8)–2.7
No. of all reflections	722,041	109,279
No. of unique reflections	59,996	10,430
Completeness (%)	95.3 (95.1)	100.0 (100.0)
Avg I/σ(I)	5.2 (3.1)	5.4 (4.8)
R_{merge}[a] (%)	13.5 (62.9)	18.7 (51.9)
Refinement statistics		
No. of reflections used ($\sigma(F) > 0$)	50,215	10,379
R_{work}[b] (%)	20.8	19.5
R_{free}[b] (%)	24.8	25.7
RMSD bond distance (Å)	0.006	0.011
RMSD bond angle (°)	1.38	1.51
Avg B value (Å^2)	33.5	30.7
Ramachandran plot (excluding Pro and Gly)		
Res. in most favored regions	276 (86.8%)	269 (84.6%)
Res. in additionally allowed regions	39 (12.3%)	45 (14.2%)
Res. in generously allowed regions	3 (0.9%)	4 (1.3%)

[a] $R_{merge} = \Sigma_h \Sigma_I I_{ih} - \langle I_h \rangle / \Sigma_h \Sigma_I \langle I_h \rangle$, where $\langle I_h \rangle$ is the mean of the observations I_{ih} of reflection h.
[b] $R_{work} = \Sigma(\|F_p(\text{observed}) - F_p(\text{calculated})\|)/\Sigma F_p(\text{observed})$. R_{free} is the R factor for a selected subset (5%) of the reflections that was not included in prior refinement calculations.
[c] Numbers in parentheses are corresponding values for the highest resolution shell.

a Fluoroskan Ascent instrument (ThermoLabsystems, Helsinki, Finland). All experiments were repeated more than three times, and representative data are shown.

Protein structure accession numbers. Coordinates and structure factors for the MHV nsp15 crystal structures have been deposited in the RCSB Protein Data Bank under accession numbers 2GTH (for the 2.7-Å WT crystal structure) and 2GTI (for the 2.15-Å F307L mutant structure).

RESULTS AND DISCUSSION

Overall structure. The cDNA coding for MHV nsp15 was cloned and amplified using PCR. The coded protein consists of amino acid residues 6506 to 6879 of pp1ab, which are renumbered 1 to 374 hereafter for convenience. The recombinant WT protein and a selenomethionyl derivative of the incidental mutant F307L were crystallized in different morphologies but with the same cell parameters and with similar structures. Unless specifically mentioned, the two crystal structures are discussed without distinction. In both crystal structures, residues in the region Tyr195-Leu216 and after Phe369 (modeled as alanine) could not be traced due to lack of interpretable electron density, although a protein sample of dissolved crystals was confirmed to be an intact peptide by sodium dodecyl sulfate-polyacrylamide gel electrophoresis analysis. Cα atom root mean square deviation (RMSD) between the two crystal structures is 0.44 Å.

Crystallographic symmetry-related nsp15 molecules form tight trimers, which further assemble into hexamers with whole symmetry D3 (Fig. 1A to C). According to the large contact surface area (discussed below), this hexamer is believed to be equivalent to the functionally required nsp15 hexamer in solution. The electrostatic potential on the hexamer surface is shown in Fig. 1D. The electrostatic surface is predominantly negative at the ends of the hexamer, with areas of positive and negative charge scattered around the sides. The dimensions of the MHV-A59 nsp15 hexamer are 96 by 96 by 110 Å, which are in excellent agreement with single-particle analysis of SARS-CoV nsp15 (9). Image reconstruction from transmission EM analysis of SARS-CoV nsp15 suggested that six subunits form a dimer of trimers with dimensions of ~90 by 90 by 110 Å. Consistent with the SARS-CoV nsp15 EM structure, our MHV-A59 nsp15 structure shows cavities at both ends as well as a central core. Nevertheless, there is no evidence of the channels observed from a side-on view of SARS-CoV nsp15.

Monomer structure of nsp15. The refined model of nsp15 consists of residues from the N terminus (including an additional serine residue from the GST tag) to Phe369. The nsp15 monomer contains nine α-helices (α1 to α9) and 21 β-strands (β1 to β21). The secondary structure elements and their locations in the primary structure are illustrated in Fig. 2. The overall fold of the nsp15 monomer can be viewed as a butterfly-shaped molecule (Fig. 2A) with approximate dimensions of 40 by 55 by 70 Å. It contains three domains: the N-terminal "wing" domain (or N-domain; residues 1 to 63), the middle "body" domain (or M-domain; residues 64 to 194), and the C-terminal "wing" domain (C-domain; residues 217 to 396). The N-terminal domain contains two α-helices (α1 and α2) and a three-strand antiparallel β-sheet (β1-β2-β3), and it is connected to the middle domain through the 60-to-69 loop. The middle domain contains one major mixed β-sheet (β4-β7-β8-β14-β9/β15), three small ones (β5-β6, β10-β11, and β12-β13), and two short α-helices (α3 and α4). Skipping the missing region from Tyr195-Leu216, which is presumably a flexible interdomain linker, the visible C-terminal domain contains two

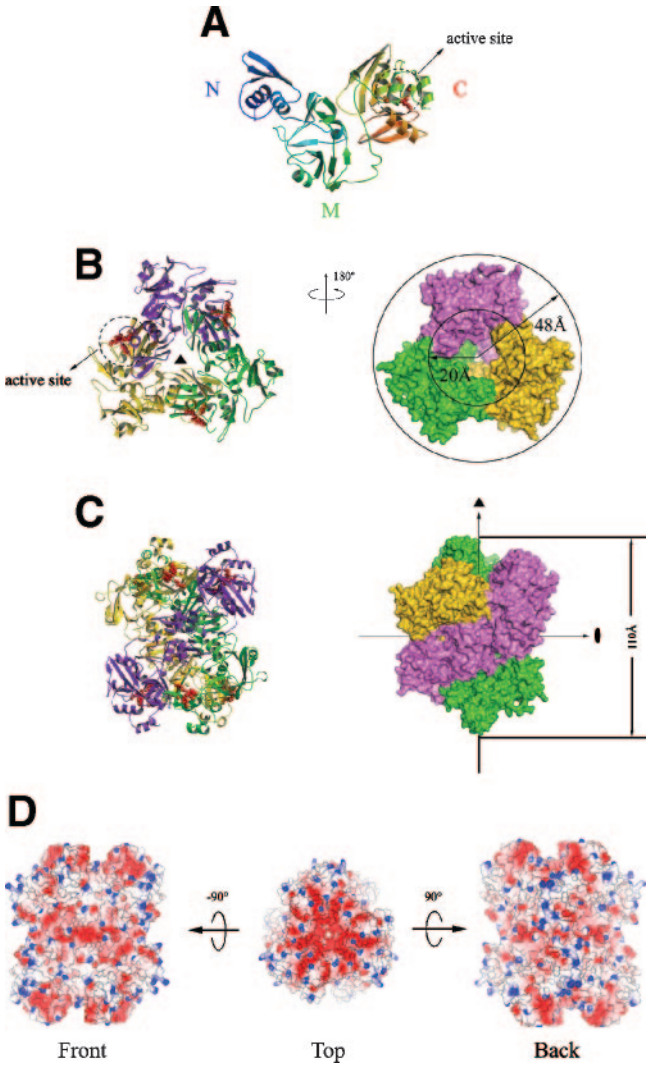

FIG. 1. Overall structure of the nsp15 hexamer assembly. A. The monomer ribbon representation. The N-terminal, middle, and C-terminal domains are labeled as N, M, and C, respectively, and are colored from blue at the N terminus to red at the C terminus. B. Ribbon (left) and molecular surface representation (right) of the nsp15 trimer. The three monomers are colored purple, green, and gold. The dimensions of the trimer as well as its cavity are noted. Putative active-site residues are shown as red spheres. C. Ribbon (left) and molecular surface representation (right) of the nsp15 hexamer. Two trimers form a hexamer through a crystallographic twofold symmetry (depicted as an oval). The threefold axis passing through the hexamer is depicted as a triangle. Also labeled is the height of the hexamer. Putative active-site residues are shown as red spheres. D. The molecular surface model of the hexamer is shown in three orientations. Electrostatic potential is mapped on the surface, with the positively charged region colored blue and the negatively charged region colored red. Panel A was drawn with the programs Bobscript (7) and Raster3D (16), panels B and C were drawn with PyMol (http://www.pymol.org/), and panel D was drawn with the program CCP4 mg (20, 21).

β-sheets (β16-β17-β18 and β19-β20-β21) and five α-helices (α5 to α9). The interface between the N-terminal and middle domains buries a solvent-accessible surface (SAS) of ~1,300 Å^2, and that between the middle and C-terminal domains buries ~1,800 Å^2. SAS calculations were performed using CCP4 (5). Such extensive interactions are likely to endow the three-domain organization of nsp15 with high stability. On the other hand, the multidomain organization provides a large surface area and structural motifs to interact with other macromolecules as well as to form a homooligomer. Three previously identified residues critical to the activity of nsp15, namely His262, His277, and Lys317, are close to each other in 3D structure and are located on a concave surface in the C-domain of one monomer, where they are distributed around the edge of a cavity (Fig. 2D). In the WT nsp15 structure, His277 $N_{\varepsilon 2}$ (3.06 Å), Lys317 N_{ζ} (3.18 Å), and Glu363 $O_{\varepsilon 2}$ (2.83 Å) all interact with a bound water molecule, while Glu363 $O_{\varepsilon 2}$ forms a hydrogen bond with His262 $N_{\varepsilon 2}$ (2.65 Å). Other strictly conserved residues distributed around the putative active site include Gly266, Gly274, Gly275, Ile280, Val319, Cys320, and Asp324. Among the nine cysteine residues in an nsp15 monomer, only Cys80 and Cys95 are potentially able to form an intramolecular disulfide bond. Nevertheless, their S_{γ}-S_{γ} distance is 4.0 Å, which is thus in the oxidized state. Interestingly, the surface loop where Cys95 resides is involved in nsp15 oligomerization; therefore, the reduced oxidation state of the potential disulfide bridge might influence the stability of the oligomer.

A whole-monomer and domain-by-domain search in DALI failed to identify any structural homologs, indicating the novelty of the MHV-A59 nsp15 structure and fold.

Monomer-monomer interactions and trimer assembly. nsp15 monomers are organized into trimers inside the crystal (Fig. 3). There are two sets of crystallographically independent threefold axes in the nsp15 crystal form, and each one assembles the nsp15 monomers into a distinct trimer. The first type of trimer buries 2,600 Å^2 SAS per monomer (54% contributed by hydrophobic groups), and the second one buries 1,400 Å^2 SAS per monomer. As a result of the more extensive monomer-monomer interactions, the first trimer is believed to be biologically relevant and will be discussed in more detail. This trimer has the shape of a three-footed pot, with the N-terminal domain forming the bottom, the C-terminal domain shaping the rim as well as three ears, and the middle domain contributing to the wall of the cavity and forming the three feet. The central spherical cavity of the trimer is about 35 to 40 Å in diameter, and the opened end is slightly smaller in diameter (~20 Å). The closed end has a hole with a diameter of less than 10 Å. The outer surface of the foot and ear from each monomer forms a continuous ridge. In such a trimer, the small N-terminal domain packs against a deep cleft between the middle and C-terminal domains (Fig. 3B). Although extensive hydrogen bond networks are observed in the monomer-monomer interface, no intermolecular β-sheet exists in the trimer. Intermonomer hydrogen bonds include those of Lys30-Asn45 (3.2 Å), Lys30-Thr47 (2.9 Å), Glu38-Arg73 (2.6 Å), Asp39-Lys90 (3.1 Å), Asn157-Thr309 (3.0 Å), Lys163-Ser313 (3.3 Å), Gly165-Ser313 (3.0 Å), and Asp166-Ser313 (2.8 Å). Residue Phe307 is located in the β17 strand and would be partially solvent exposed in a monomer. In both the WT and F307L crystals, however, the side chain at this position becomes completely buried in the trimer interface and faces Ile63 from a neighboring monomer.

Trimer-trimer interactions and hexamer architecture. Two nsp15 trimers of the type described above further interact in a base-to-base fashion to form a hexamer through crystallographic twofold symmetries (Fig. 1). The two sets of three feet

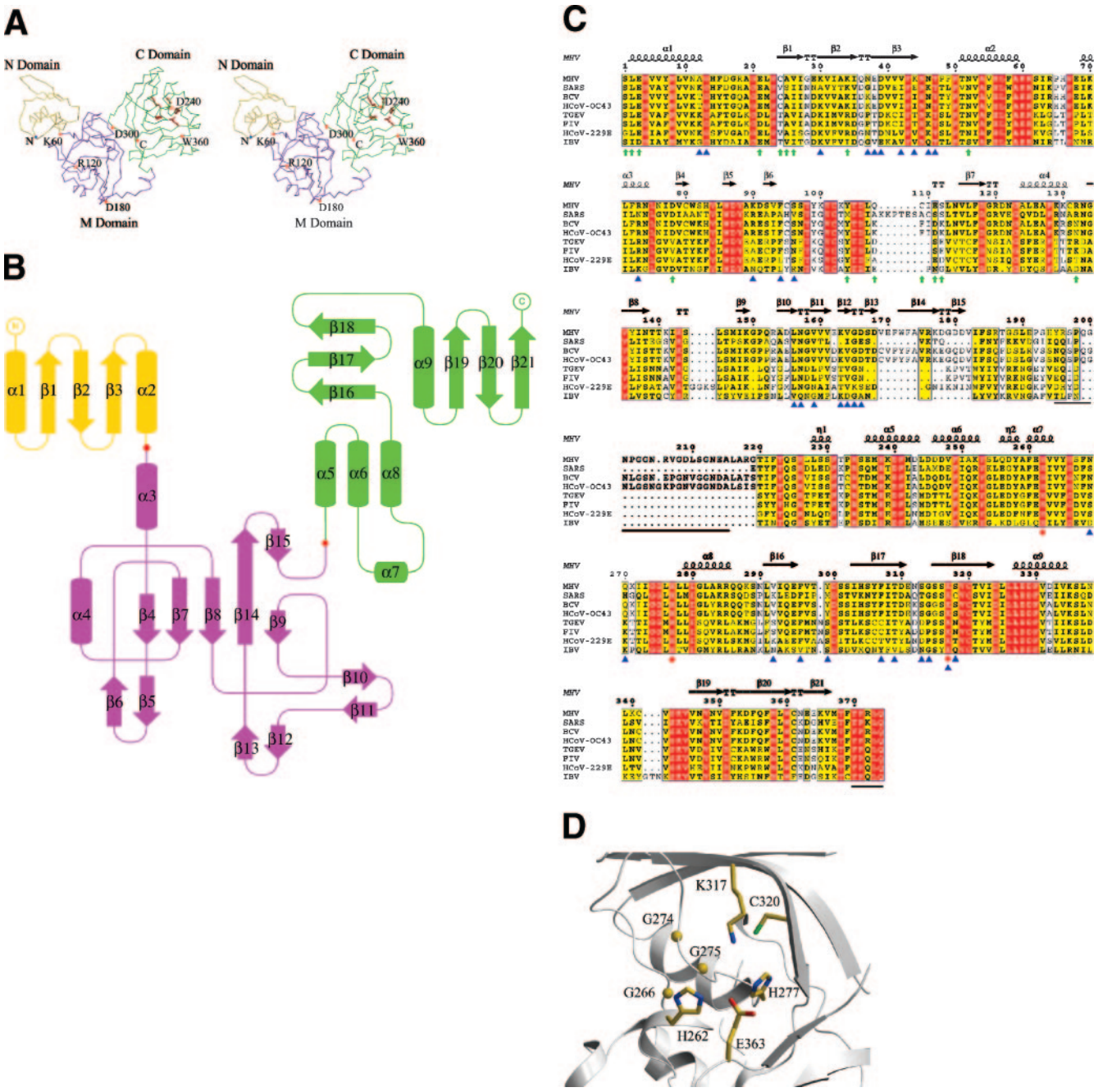

FIG. 2. Structure of the nsp15 monomer. A. Stereo view of the nsp15 monomer Cα backbone trace. The N-terminal "wing" (N) domain (residues 1 to 63) is colored gold, the middle "body" (M) domain (residues 64 to 194) is colored magenta, and the C-terminal "wing" (C) domain is colored green. Positions of selected residues and the N and C termini are labeled, and putative active-site residues are shown in red. B. Topology of the nsp15 monomer. β-Strands are shown with arrows, and α-helices are shown with cylinders. The color scheme is similar to that of panel A. C. Multiple-sequence alignment of MHV-A59 nsp15 with representatives from all three groups of the genus *Coronavirus*. MHV, mouse hepatitis virus strain A59; SARS, severe acute respiratory syndrome; BCV, bovine coronavirus; HCoV-OC43, human coronavirus strain OC43; TGEV, porcine transmissible gastroenteritis virus; FIV, feline infectious peritonitis virus; HCoV-229E, human coronavirus strain 229E; and IBV, avian infectious bronchiolitis virus. Secondary structural elements of the MHV-A59 nsp15 crystal structure are shown at the top of the alignment; arrows indicate β-strands, and helical curves denote α- or 3_{10}-helices. Residues highlighted in red are identical among the compared proteins; residues highlighted in yellow are conserved. The three putative active-site residues are marked with red asterisks. Residues important for trimer stability and hexamer formation are marked with blue triangles and green vertical arrows, respectively. Residues missing from the current crystal structure are underlined. The alignment was generated using the program ClustalX (28) and drawn with ESPript (8). D. The putative nsp15 active site. The nsp15 structure is shown in ribbon representation and is colored gray. The proposed active-site residues His262, His277, and Lys317 are shown in stick representations, together with other conserved residues lining the cavity. Carbon, nitrogen, oxygen, and sulfur atoms are colored yellow, blue, red, and green, respectively.

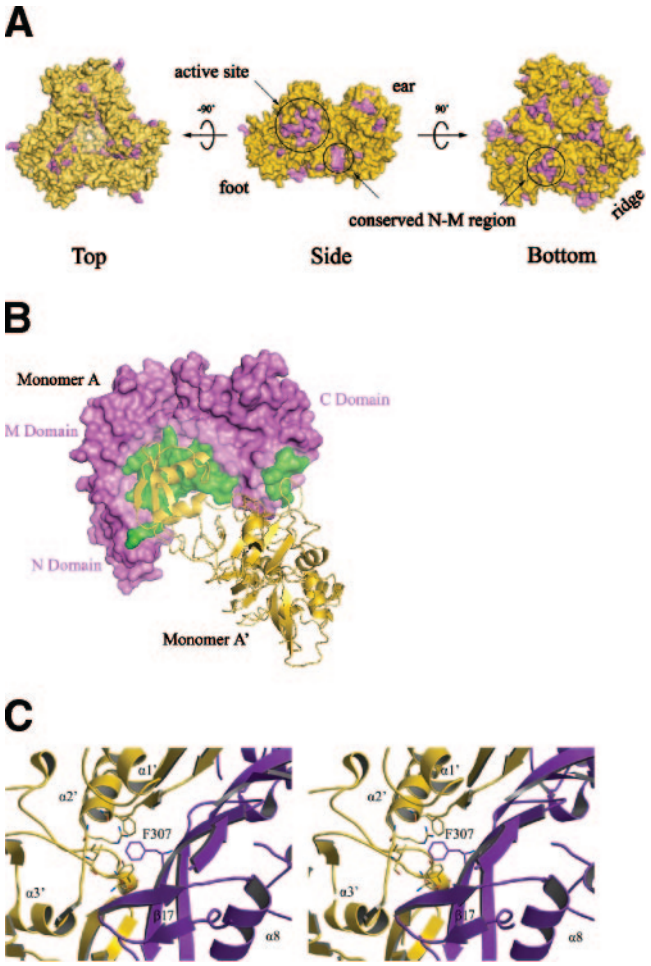

FIG. 3. Trimer organization of nsp15. A. A molecular surface representation of the nsp15 trimer shown in three orientations. The surface is shown in gold, with strictly conserved residues from the sequence alignment (Fig. 2C) colored purple. Some structural features, including the putative active site, are labeled. B. Monomer-monomer packing. Two monomers (denoted A and A′) in a trimer are illustrated as a molecular surface model and a ribbon model, respectively. Two interacting regions in the molecular surface model are highlighted in green. C. Stereo view of the 307-position region. One monomer is colored purple, and the other is colored gold. The peptide backbone is shown in a ribbon representation, and selected residues are shown as stick models.

are slightly displaced relative to each other, if viewed along the crystallographic threefold axis shared by the two trimers. The trimer-trimer interface buries 3,600 Å^2 SAS from each trimer, with 47% contributed by nonpolar groups. Around the waist of the hexamer, Cys109 from each nsp15 monomer forms a twofold symmetry-restricted disulfide bond with its counterpart across the trimer-trimer interface. Deep in the center of the hexamer, the helix α1 at each N terminus goes face to face following another crystallographic twofold symmetry with its counterpart to form a close contact. An extensive expansion of the nsp15 N terminus should prohibit the formation of the hexamer, which is consistent with the observation that all known nsp15 proteins have uniform N termini. As in the monomer-monomer interface within a trimer, no intermolecular β-sheet exits in the trimer-trimer interface. The visible C terminus (residue 369) is located near both the intermonomer and intertrimer interfaces, but it is buried in neither. Similarly, the missing region of Tyr195-Leu216 is projected to be on the surface of the hexamer. This flexible region is unlikely to interfere with either the trimer or hexamer formation. Furthermore, this region is located on the opposite side of the C-terminal domain from where the putative active-site residues His262, His277, and Lys317 cluster together.

A detailed analysis of the distribution of conserved residues in the nsp15 structure further supports the biological relevance of the crystallographically observed hexamer. Figure 2C shows high sequence homology among CoV nsp15 proteins. For simplicity, we focus on the strictly conserved residues in the sequence alignment. Most of the identical residues are concentrated in two regions in the 3D structure of nsp15: (i) the interface between the N-terminal and middle domains (conserved N-M region) and (ii) the C-terminal domain. The first region is heavily involved in both trimer and hexamer formation; therefore, these conserved residues play important roles in several levels of nsp15 structural organization. The tip of the N-terminal domain, however, is not the most conserved region. Nevertheless, during the trimer formation it forms a complementary interaction with an equally less conserved concave surface area formed by the middle and C-terminal domains. On the other hand, most of the conserved C-terminal domain residues do not directly participate in intermonomer contacts. The largest cluster of conserved residues in the C-terminal domain forms the top face of the pot and the entry rim. In nsp15, the top face of this cluster and its surrounding region are particularly rich in acidic residues, including Glu236, Asp240, Asp243, Asp245, Asp246, Asp247, Glu261, Asp328, and Asp329. Another 3D cluster of conserved residues in the C-domain consists of the three above-mentioned key residues in catalysis (i.e., His262, His277, and Lys317) and their surrounding region. Furthermore, the highly conserved but mobile C-terminal tail is close to the putative active site and may also play a functional role in catalysis.

Regarding the structural basis for the requirement of oligomerization for the enzymatic activity (see below), we have identified an extended patch on the hexamer surface of concentrated conserved residues. It starts from the putative active site on one C-terminal domain, extends across the conserved N-M region in a neighboring molecule in the trimer, and further spans across the trimer-trimer interface via a crystallography twofold symmetry. The hexamer formation may enhance the enzyme activity in one of at least two possible ways: (i) the extended conserved surface patch facilitates the substrate recognition, and (ii) the catalytic machinery is composed of parts from different domains that are brought together in the hexamer.

Besides the conserved residues, the sequence deletion-insertion pattern shown in Fig. 2C is also consistent with our structure-based observations. There are six deletion-insertion regions among the CoV nsp15 proteins compared in Fig. 2C. Four of them (around positions 174, 145, 210, and 340) align on the outer surface ridge, including the Tyr195-Leu216 region mobile inside the crystal; the fifth one, near position 229, is at the toe of the pot foot; and the last one is near position 298 and is located inside the pot cavity. All six deletion-insertion regions are solvent exposed and unlikely to interfere with the

trimer and hexamer organization of nsp15 in any of the coronaviruses included in the comparison. In addition, these variable regions are in locations distinct from the putative active site. Furthermore, most of the deletion-insertion segments are in regions of non-α, non-β secondary structure, except the one located in the β14-β15 turn. In the MHV-A59 nsp15 crystal structure, this β-turn protrudes into solvent. Removing this β-turn would not compromise the stability of the monomer or higher order oligomers.

Mn^{2+} dependence of the endoribonuclease activity and catalytic residues. To verify that our recombinant nsp15 has RNA substrate specificity, we performed an enzyme activity assay for two substrates that differ in only one nucleotide. For an enzyme concentration of 0.2 μM and substrate concentration of 1.2 μM, the reaction velocity of 5′-FAM-dC-rU-dA-dA-3′-TAMRA hydrolysis is 1.8 (±0.22) nM s^{-1}, while 5′-FAM-dC-dT-dA-dA-3′-TAMRA was not cleaved by the enzyme, indicating that nsp15 is uridine specific and has no hydrolysis activity against deoxythymidine. Since the only chemical differences between the two substrates were deoxythymidine C5 methylation and C2′ deoxidation, the discrepancy in the enzyme activities for the two substrates is likely to stem from the C5 methyl and C2′ hydroxyl groups. Furthermore, based on previous studies on NendoU in which the C2′ hydroxyl group played a critical role in substrate cleavage (10), we propose that the 2′ hydroxyl group is also involved in the nsp15-catalyzed hydrolysis reaction.

It has been proposed that the endoribonuclease activity of coronavirus nsp15 is Mn^{2+} dependent, although the structural basis of this dependence remains unclear. Enzyme activity assays were performed with 0.25 μM WT nsp15 and 1 μM 5′-FAM-dC-rU-dA-dA-3′-TAMRA substrate in the presence of various concentrations of manganese. The enzyme activity increased linearly when the concentration of Mn^{2+} was increased from 1 to 5 mM. These results indicate that the MHV-A59 nsp15 is a manganese-enhanced uridine-specific endoribonuclease.

We further performed enzyme activity assays for WT nsp15 and the H262S, H277S, and K317S mutants under identical conditions. With the concentration of enzyme at 0.25 μM and that of the substrate 5′-FAM-dC-rU-dA-dA-3′-TAMRA at 1 μM, the activity of the mutants was at least 10-fold less than that of the WT one monitored using fluorescent absorption at 518 nm (Fig. 4A). Thus, the H262S, H277S, and K317S mutations severely diminish the enzyme activity, revealing that these three residues are located at a catalytic site. Previous studies of similar mutations in SARS-CoV nsp15 and NendoU suggest that a decrease in their ion binding or substrate binding capacity may be an additional or alternative reason for the loss of endoribonuclease activity (9, 10).

The close proximity of His262, His277, and Lys317 around a cavity suggests that they may coordinate a manganese ion. In order to verify if this region is the manganese binding site, we attempted to soak MHV-A59 nsp15 crystals with manganese. In a resulting 2.5-Å structure, while there appeared to be strong electron density in the cavity supporting a bound metal ion, we did not observe the expected hexacoordination environment for manganese (data not shown). Furthermore, inspection of the crystal structure does not suggest that Mn^{2+} binding is disrupted by the crystal packing.

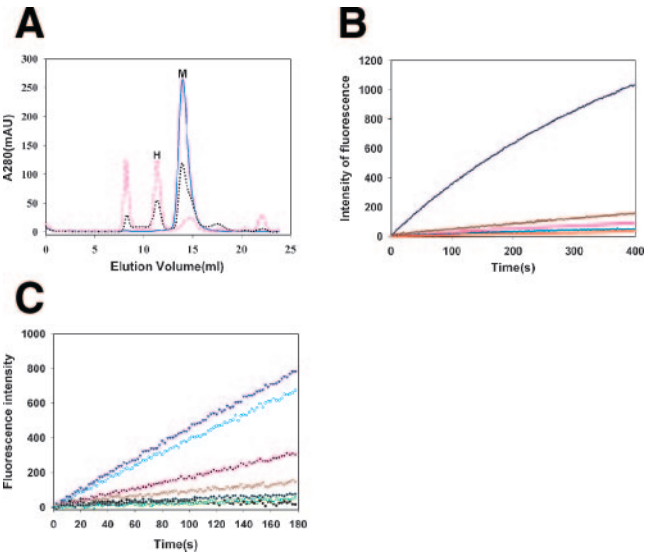

FIG. 4. Gel filtration and activity analyses of MHV-A59 nsp15. (A) Gel filtration analysis of nsp15 variants. The WT and H262S, H277S, K317S, and F307L variants were loaded at 500-μg quantity separately and eluted at 0.5 ml min^{-1} with a buffer containing 25 mM Tris-HCl (pH 8.0), 150 mM NaCl, 1 mM DTT. WT measurements are represented with a dashed pink line, F307 with a solid blue line, and H277 with a dotted black line. The WT was eluted in three peaks corresponding to random aggregation, hexamer (H), and monomer (M), respectively; in contrast, F307L was dominated by the monomer, and the H262S, H277S, and H317S mutants exhibited an in-between level of aggregation. For clarity, the elution profiles of the mutants H262S and H317S are not shown, since they are similar to that of H277S. (B) FRET-based enzyme activity assay. The assay was performed with 0.25 μM enzyme and 1 μM fluorescent substrate. The reaction mixture was placed in a 30°C water bath for 5 s, and absorption at 518 nm was recorded every 2 s for 400 s. WT measurements are represented in blue, H262S in pink, H277S in cyan, K317S in dark red, and F307L in red. Among them, the WT is the most active, H262S and K317S are marginally active, and H277S and F307L are inactive. (C) The effect of Mn^{2+} on enzyme activity of WT and F307L. The FRET-based enzyme activity assays were carried on for 200 s in the presence or absence of 5 mM Mn^{2+}. Data for WT nsp15 hexamer species with Mn^{2+} are presented in blue, and those without Mn^{2+} are in cyan; WT monomer data with Mn^{2+} are in pink, without Mn^{2+} are in dark red; F307L data without Mn^{2+} are in green, with Mn^{2+} are in dark green. A control experiment was performed without enzyme and Mn^{2+} and is presented as black dots.

MHV-A59 nsp15 is fully active only as a hexamer. Elution of purified MHV-A59 WT nsp15 by gel filtration yields three distinct 280-nm absorption peaks (Fig. 4B). The first peak was eluted at 8.2 (±0.1) ml and is believed to be a random aggregation state with no biological function, since this species has no enzymatic activity and could not be crystallized. According to the elution pattern of the Pharmacia standard marker proteins (data not shown), the second peak was eluted at 11.4 (±0.1) ml, corresponding to a molecular weight consistent with a hexamer of nsp15. The third peak appeared at 14.9 (±0.2) ml, corresponding to the monomer of nsp15. The areas under the first and second peaks are larger than that under the third one (Fig. 4B). Interestingly, the equilibrium between the three peaks of MHV-A59 nsp15 was not affected by Mn^{2+} concentration or reducing agents such as DTT. In contrast to MHV-A59 nsp15, it was shown previously that, under similar condi-

tions, SARS-CoV nsp15 exhibits two distinct UV absorption peaks at 11.41 ml and 15.1 ml, respectively, and 90% of the total protein was hexameric (9). When performed with the same 500-μg quantity of enzyme under identical conditions, the elution profiles of H262S, H277S, and K317S mutants were similar to that of the WT nsp15. Each mutant was eluted at three distinct 280-nm absorption peaks, with the second peak appearing at 11.4 (±0.1) ml and the third peak appearing at 14.6 (±0.7) ml (H277S is shown in Fig. 4A). However, the detailed ratio of the three peaks was different between the three mutants and WT nsp15. Thus, replacement of His262, His277, and Lys317 with serine did not influence hexamer formation in solution. The lower activity of these active-site mutants does not result from the different proportions of oligomeric species but from disruption of the catalytic site. In addition, based on the structure, these active catalytic site residues do not participate in interactions between monomers.

The F307L mutant is detrimental to endoribonuclease activity. Under the same conditions as those for WT nsp15, the activity of the F307L mutant was extremely low and showed no response to Mn^{2+}. Meanwhile, unlike other low-activity mutants being analyzed, the elution profile of the F307L mutant through a Superdex 200 gel filtration column is in sharp contrast to that of the WT nsp15. Two peaks were observed at 8.3 (±0.1) ml and 14.0 (±0.1) ml, respectively, and the first peak was much weaker (15%) than the monomer peak eluted later (85%) (Fig. 4B). Thus, the F307L mutant exists in two forms, with the second peak being the dominant species in the buffer. This species corresponds to a molecular mass of about 72 kDa and may be a mixture of monomer, dimer, and trimer. These results suggest that the cause of activity loss in the F307L mutant is different from that of active-site mutations. Since Phe307 is buried within the trimer interface, replacement of Phe307 with leucine may disturb the hydrophobic interactions between two monomers, preventing the formation of stable trimers and hexamers. It appears that the crystallization process of F307L selected the trimer form for crystal packing, thus shifting the equilibrium between species.

To further clarify the relationship between hexamer formation and activity, we performed enzyme activity assays for the hexamer and monomer species of WT nsp15 separately after collecting the elution fractions. Since we did not observe the WT trimer species from gel filtration experiments, activity of the trimer could not be assayed. The dynamic parameters for the hexamer species are the following: K_m, 24 ± 3.5 μM; k_{cat}, 0.20 ± 0.03 s^{-1}; for the monomer species they are the following: K_m, 27 ± 3 μM; k_{cat}, 0.20 ± 0.02 s^{-1}. The k_{cat} values for the hexamer and monomer species are identical, indicating their catalytic activities are the same, but the K_m value for the hexamer is slightly lower than that for the monomer, suggesting its substrate binding ability may be slightly greater than that of the monomer species. Furthermore, the activity of WT nsp15 can be enhanced by the presence of Mn^{2+} (Fig. 4C). Therefore, we conclude that the full activity of nsp15 requires a stable hexamer formation, which is believed to favor substrate binding. This notion is strongly supported by the results from our crystallography analysis on the structure of nsp15 hexamer. Consistent with this rationale, previous studies concerning SARS nsp15 also point to the hexamer as the enzymatically active state (9). In contrast to the three active-site mutants, SARS CoV nsp15 E56A (56 in MHV) and D212A (240 in MHV) point mutants behave the same as the WT in both gel filtration and activity assays, while E3A (3 in MHV) shows a larger monomer population (52%) and lower level of activity. Inspection of equivalent positions in the crystal structure of MHV-A59 nsp15 provides a clear explanation to the varied functional behaviors of these mutants at conserved positions throughout the coronavirus family. Both Glu56 and Asp240 are located on the monomer surface and are not directly involved in oligomerization, while the side chain of Glu3 forms a 2.9-Å hydrogen bond with the main-chain amide nitrogen of Leu2 of the nsp15 monomer across the trimer-trimer interface. Thus, this observation once again confirms that hexamerization is important for nsp15 activity. Furthermore, the activity of the D212A mutant indicates that the corresponding ear region in the hexamer is less likely to contribute to the enzymatic activity.

Conclusions. The scientific significance of this study is as follows. First, the crystal structure of MHV-A59 nsp15 demonstrates a new protein fold. Second, the MHV-A59 nsp15 structure provides a model for elucidation of the structure-function relationship in the XendoU family. It becomes the first member of this family to have its 3D structure unveiled. Other members of this family are likely to share the same novel fold and organization. Third, we firmly demonstrate that the specific catalysis of nsp15 at the uridine nucleotide depends both on stable hexamer formation and Mn^{2+} ion binding. Mutations disturbing the monomer-monomer interface are detrimental to the activity of nsp15. Fourth, the conserved amino acids His262, His277, and Lys317 constitute the active-site residues and are critical for the enzyme activity of nsp15. Endoribonuclease activity is essential for the virus life cycle and is unusual among positive-strand RNA viruses. The high sequence conservation of the nsp15 enzyme in coronaviruses, including SARS, provides a new potential avenue for the design of antiviral therapeutics. One possibility may be to use an approach similar to the design of broad-spectrum coronavirus M^{pro} inhibitors in which a conserved region of the enzyme was targeted (29). The current studies on MHV-A59 nsp15 provide rich structural information for the development of inhibitors and other antiviral drugs. The 3D structure of MHV-A59 nsp15 also adds to the increasing knowledge base of coronavirus replicase/transcriptase structures (2), which also includes the SARS-CoV nsp3 ADRP domain (22), SARS-CoV nsp5 (M^{pro}) (2), the hexadecameric SARS-CoV nsp7-nsp8 complex (32), SARS-CoV nsp9 (6, 26), and SARS-CoV nsp10 (Z. Rao, personal communication).

ACKNOWLEDGMENTS

We thank Haitao Yang, Xiaoyu Xue, Feiran Zhang, Sifei Xing, Xiaorui Chen, Jun He, Sheng Ye, and Yi Han for technical assistance.

This work was supported by Project 973 of the Ministry of Science and Technology of China (grant number 2004CB720000), the NSFC (grant number 30221003), the Sino-German Center (grant number GZ236[202/9]), and the "Sino-European Project on SARS Diagnostics and Antivirals" (SEPSDA) of the European Commission (grant number 003831).

REFERENCES

1. **Baker, S. C., C. K. Shieh, L. H. Soe, M. F. Chang, D. M. Vannier, and M. M. Lai.** 1989. Identification of a domain required for autoproteolytic cleavage of murine coronavirus gene A polyprotein. J. Virol. **63:**3693–3699.

2. **Bartlam, M., H. Yang, and Z. Rao.** 2005. Structural insights into SARS coronavirus proteins. Curr. Opin. Struct. Biol. **15:**664–672.
3. **Bhardwaj, K., L. Guarino, and C. C. Kao.** 2004. The severe acute respiratory syndrome coronavirus nsp15 protein is an endoribonuclease that prefers manganese as a cofactor. J. Virol. **78:**12218–12224.
4. **Brunger, A. T., P. D. Adams, G. M. Clore, W. L. DeLano, P. Gros, R. W. Grosse-Kunstleve, J. S. Jiang, J. Kuszewski, M. Nilges, N. S. Pannu, R. J. Read, L. M. Rice, T. Simonson, and G. L. Warren.** 1998. Crystallography and NMR system: a new software suite for macromolecular structure determination. Acta Crystallogr. Sect. D Biol. Crystallogr. **54:**905–921.
5. **Collaborative Computational Project, N.** 1994. The CCP4 suite: programs for protein crystallography. Acta Crystallogr. Sect. D Biol. Crystallogr. **50:** 760–763.
6. **Egloff, M. P., F. Ferron, V. Campanacci, S. Longhi, C. Rancurel, H. Dutartre, E. J. Snijder, A. E. Gorbalenya, C. Cambillau, and B. Canard.** 2004. The severe acute respiratory syndrome-coronavirus replicative protein nsp9 is a single-stranded RNA-binding subunit unique in the RNA virus world. Proc. Natl. Acad. Sci. USA **101:**3792–3796.
7. **Esnouf, R. M.** 1997. An extensively modified version of MolScript that includes greatly enhanced coloring capabilities. J. Mol. Graph Model **15:** 112–134.
8. **Gouet, P., X. Robert, and E. Courcelle.** 2003. ESPript/ENDscript: extracting and rendering sequence and 3D information from atomic structures of proteins. Nucleic Acids Res. **31:**3320–3323.
9. **Guarino, L. A., K. Bhardwaj, W. Dong, J. Sun, A. Holzenburg, and C. Kao.** 2005. Mutational analysis of the SARS virus nsp15 endoribonuclease: identification of residues affecting hexamer formation. J. Mol. Biol. **353:**1106–1117.
10. **Ivanov, K. A., T. Hertzig, M. Rozanov, S. Bayer, V. Thiel, A. E. Gorbalenya, and J. Ziebuhr.** 2004. Major genetic marker of nidoviruses encodes a replicative endoribonuclease. Proc. Natl. Acad. Sci. USA **101:**12694–12699.
11. **Jones, T. A., J. Y. Zou, S. W. Cowan, and L. Kjeldgaard.** 1991. Improved methods for building protein models in electron density maps and the location of errors in these models. Acta Crystallogr. Sect. A **47:**110–119.
12. **Laneve, P., F. Altierei, M. E. Fiori, A. Scaloni, I. Bozzoni, and E. Caffarelli.** 2003. Purification, cloning, and characterization of XendoU, a novel endoribonuclease involved in processing of intron-encoded small nucleolar RNAs in Xenopus laevis. J. Biol. Chem. **278:**13026–13032.
13. **Matthews, A. E., E. Lavi, S. R. Weiss, and Y. Paterson.** 2002. Neither B cells nor T cells are required for CNS demyelination in mice persistently infected with MHV-A59. J. Neurovirol. **8:**257–264.
14. **Matthews, A. E., S. R. Weiss, and Y. Paterson.** 2002. Murine hepatitis virus—a model for virus-induced CNS demyelination. J. Neurovirol. **8:**76–85.
15. **Matthews, B. W.** 1968. Solvent content of protein crystals. J. Mol. Biol. **33:**491–497.
16. **Merritt, E. A., and D. J. Bacon.** 1997. Raster3D: photorealistic molecular graphics. Methods Enzymol. **277:**505–524.
17. **Miyashiro, H., T. Kimura, M. Tomiyama, and M. Hattori.** 2000. Analysis of the RNase H activity by fluorescence resonance energy transfer. Nucleic Acids Symp. Ser. **44:**55–56.
18. **Otwinowski, Z., and W. Minor.** 1997. Processing of X-ray diffraction data collected in oscillation mode, p. 307–326. *In* C. W. Carter, Jr., and R. M. Sweet (ed.), Macromolecular crystallography, part A, vol. 276. Academic Press, New York, N.Y.
19. **Perrakis, A., R. M. Morris, and V. S. Lamzin.** 1999. Automated protein model building combined with iterative structural refinement. Nat. Struct. Biol. **6:**458–463.
20. **Potterton, E., S. McNicholas, E. Krissinel, K. Cowtan, and M. Noble.** 2002. The CCP4 molecular-graphics project. Acta Crystallogr. Sect. D Biol. Crystallogr. **58:**1955–1957.
21. **Potterton, L., S. McNicholas, E. Krissinel, J. Gruber, K. Cowtan, P. Emsley, G. N. Murshudov, S. Cohen, A. Perrakis, and M. Noble.** 2004. Developments in the CCP4 molecular-graphics project. Acta Crystallogr. Sect. D Biol. Crystallogr. **60:**2288–2294.
22. **Saikatendu, K. S., J. S. Joseph, V. Subramanian, T. Clayton, M. Griffith, K. Moy, J. Velasquez, B. W. Neuman, M. J. Buchmeier, R. C. Stevens, and P. Kuhn.** 2005. Structural basis of severe acute respiratory syndrome coronavirus ADP-ribose-1′-phosphate dephosphorylation by a conserved domain of nsP3. Structure (Cambridge) **13:**1665–1675.
23. **Snijder, E. J., P. J. Bredenbeek, J. C. Dobbe, V. Thiel, J. Ziebuhr, L. L. Poon, Y. Guan, M. Rozanov, W. J. Spaan, and A. E. Gorbalenya.** 2003. Unique and conserved features of genome and proteome of SARS-coronavirus, an early split-off from the coronavirus group 2 lineage. J. Mol. Biol. **331:**991–1004.
24. **Stryer, L.** 1978. Fluorescence energy transfer as a spectroscopic ruler. Annu. Rev. Biochem. **47:**819–846.
25. **Stryer, L., and R. P. Haugland.** 1967. Energy transfer: a spectroscopic ruler. Proc. Natl. Acad. Sci. USA **58:**719–726.
26. **Sutton, G., E. Fry, L. Carter, S. Sainsbury, T. Walter, J. Nettleship, N. Berrow, R. Owens, R. Gilbert, A. Davidson, S. Siddell, L. L. Poon, J. Diprose, D. Alderton, M. Walsh, J. M. Grimes, and D. I. Stuart.** 2004. The nsp9 replicase protein of SARS-coronavirus, structure and functional insights. Structure (Cambridge) **12:**341–353.
27. **Terwilliger, T. C.** 2000. Maximum-likelihood density modification. Acta Crystallogr. Sect. D Biol. Crystallogr. **56:**965–972.
28. **Thompson, J. D., T. J. Gibson, F. Plewniak, F. Jeanmougin, and D. G. Higgins.** 1997. The CLUSTAL_X windows interface: flexible strategies for multiple sequence alignment aided by quality analysis tools. Nucleic Acids Res. **25:**4876–4882.
29. **Yang, H., W. Xie, X. Xue, K. Yang, J. Ma, W. Liang, Q. Zhao, Z. Zhou, D. Pei, J. Ziebuhr, R. Hilgenfeld, K. Y. Yuen, L. Wong, G. Gao, S. Chen, Z. Chen, D. Ma, M. Bartlam, and Z. Rao.** 2005. Design of wide-spectrum inhibitors targeting coronavirus main proteases. PLoS Biol. **3:**e324.
30. **Yang, H., M. Yang, Y. Ding, Y. Liu, Z. Lou, Z. Zhou, L. Sun, L. Mo, S. Ye, H. Pang, G. F. Gao, K. Anand, M. Bartlam, R. Hilgenfeld, and Z. Rao.** 2003. The crystal structures of severe acute respiratory syndrome virus main protease and its complex with an inhibitor. Proc. Natl. Acad. Sci. USA **100:** 13190–13195.
31. **Yount, B., M. R. Denison, S. R. Weiss, and R. S. Baric.** 2002. Systematic assembly of a full-length infectious cDNA of mouse hepatitis virus strain A59. J. Virol. **76:**11065–11078.
32. **Zhai, Y., F. Sun, X. Li, H. Pang, X. Xu, M. Bartlam, and Z. Rao.** 2005. Insights into SARS-CoV transcription and replication from the structure of the nsp7-nsp8 hexadecamer. Nat. Struct. Mol. Biol. **12:**980–986.
33. **Zuniga, S., I. Sola, S. Alonso, and L. Enjuanes.** 2004. Sequence motifs involved in the regulation of discontinuous coronavirus subgenomic RNA synthesis. J. Virol. **78:**980–994.